

Article

An Ethyl-Thioglycolate-Functionalized Fe₃O₄@ZnS Magnetic Fluorescent Nanoprobe for the Detection of Ag⁺ and Its Applications in Real Water Solutions

Xin Chen ¹, Jie Chen ², Mingshuo Ma ², Shihua Yu ¹ , Zhigang Liu ^{2,*} and Xiaodan Zeng ^{2,*}

¹ School of Chemical and Pharmaceutical Engineering, Jilin Institute of Chemical Technology, Jilin 132022, China; chenxin92@jlicet.edu.cn (X.C.); ysh@jlicet.edu.cn (S.Y.)

² Center of Characterization and Analysis, Jilin Institute of Chemical Technology, Jilin 132022, China; jiechendr@163.com (J.C.); naya221@163.com (M.M.)

* Correspondence: lzg@jlicet.edu.cn (Z.L.); jiangzxd@163.com (X.Z.)

Abstract: Ethyl-thioglycolate-modified Fe₃O₄@ZnS nanoparticles (Fe₃O₄@ZnS-SH) were successfully prepared using a simple chemical precipitation method. The introduction of ethyl thioglycolate better regulated the surface distribution of ZnS, which can act as a recognition group and can cause a considerable quenching of the fluorescence intensity of the magnetic fluorescent nanoprobe, Fe₃O₄@ZnS-SH. Benefiting from stable fluorescence emission, the magnetic fluorescent nanoprobe showed a highly selective fluorescent response to Ag⁺ in the range of 0–400 μM, with a low detection limit of 0.20 μM. The magnetic fluorescent nanoprobe was used to determine the content of Ag⁺ in real samples. A simple and environmentally friendly approach was proposed to simultaneously achieve the enrichment, detection, and separation of Ag⁺ and the magnetic fluorescent nanoprobe from an aqueous solution. These results may lead to a wider range of application prospects of Fe₃O₄ nanomaterials as base materials for fluorescence detection in the environment.

Keywords: zinc sulfide; Fe₃O₄; nanoparticle; fluorescence



Citation: Chen, X.; Chen, J.; Ma, M.; Yu, S.; Liu, Z.; Zeng, X. An Ethyl-Thioglycolate-Functionalized Fe₃O₄@ZnS Magnetic Fluorescent Nanoprobe for the Detection of Ag⁺ and Its Applications in Real Water Solutions. *Nanomaterials* **2023**, *13*, 1992. <https://doi.org/10.3390/nano13131992>

Academic Editor: Antonios Kelarakis

Received: 31 May 2023

Revised: 26 June 2023

Accepted: 26 June 2023

Published: 1 July 2023



Copyright: © 2023 by the authors. Licensee MDPI, Basel, Switzerland. This article is an open access article distributed under the terms and conditions of the Creative Commons Attribution (CC BY) license (<https://creativecommons.org/licenses/by/4.0/>).

1. Introduction

Silver, an important transition metal, is of great commercial value and has marked antibacterial properties, meaning that it is usually used in high-strength and high-corrosion-resistance alloys and jewelry, dental and pharmaceutical preparations, and implanted prostheses [1,2]. As an important noble metal, silver is also widely used in the electronics industry as well as electroplating. In addition, soluble silver compounds and colloidal silver are usually used for treating some diseases, i.e., gastroenteritis and infections, because of their antibacterial activity. The silver content in environmental matrices is increasing with the widespread use of silver-containing compounds in procedures in medicine, industry, and so on [3].

On the other hand, silver ions (Ag⁺) are one of the most toxic heavy metals [4]. They not only cause irreversible damage to the human body, animals, and plants, but also cause great harm to water and the environment. The limit for Ag⁺ in drinking water is 0.1 mg/L or 0.93 μM based on the U.S. EPA [5]. Therefore, monitoring and detecting Ag⁺ are of great significance in environmental water, food, agricultural products, and so on.

Well-known and commonly used methods for trace Ag⁺ analysis include inductively coupled plasma mass spectrometry [6], electrochemiluminescence [7], flow injection–flame atomic absorption spectrometry [8], ICP-MS [9], the electrochemical method [10], and laser ablation microwave plasma torch optical emission spectrometry [11]. These methods can offer wide linearity ranges, low detection limits, and excellent precision. However, these methods are often easily affected by the introduction of sample solutions, leading to low measurement sensitivity and result accuracy.

The fluorescence technique [12–14] has been an attractive research tool due to its high selectivity and sensitivity, straightforward equipment requirements, and ease of operation. Many fluorescent probes have been developed, including small organic molecules [15–17], noble metal nanoclusters [18–20], quantum dots [21–23], and carbon nanodots [24,25]. In particular, quantum dots attract significant attention from chemists as a new class of inorganic fluorophores due to their unique superior properties compared to classical organic fluorophores [26–28]. Functionalization is an effective method for improving fluorescence selectivity and sensitivity. Several types of quantum dots used as sensor probes for the detection of Ag^+ have been reported [29–31]. However, the reported probes were difficult to separate from the environment completely or worked via the fluorescence-quenching approach, which was frequently caused by many possible species—especially heavy metal ions—which leads to low selectivity, introduces pollution, and hinders their application in actual environmental detection. In addition, the enrichment and separation of a fluorescent probe and target are still difficult. Therefore, it still remains challenging to develop a facile method to detect heavy ions with high fluorescence sensitivity and less pollution.

Fe_3O_4 is a class of nanoparticle that has been widely studied for its super paramagnetic properties, high surface area, easy preparation and separation, high adsorption ability, and biocompatibility [32–36]. More importantly, its ease of function features may provide it with promising applications in fluorescence detection [37–39]. From the discussion above, the introduction of Fe_3O_4 into a nanostructure is expected to provide better enrichment, detection, and separation effects and higher sensitivity. Therefore, the magnetic technique combined with fluorescent molecules can overcome the disadvantages described above.

To address the above challenges, based on the strong coordination capacity of ethyl thioglycolate groups with Ag^+ , a novel magnetic fluorescence nanoprobe ($\text{Fe}_3\text{O}_4@\text{ZnS-SH}$, Figure 1a) was prepared through a simple chemical precipitation process. Because the fluorescence intensity of the magnetic fluorescence nanoprobe was remarkably quenched by the silver ions, a fluorescence method for the determination of Ag^+ was established. In addition, the magnetic fluorescence nanoprobe was used for the determination of Ag^+ water samples successfully. The magnetic fluorescence nanoprobe combines the advantages of fluorescence analysis and magnetic separation (Figure 1b). It provided a simple, highly selective, and less polluting method to determine Ag^+ .

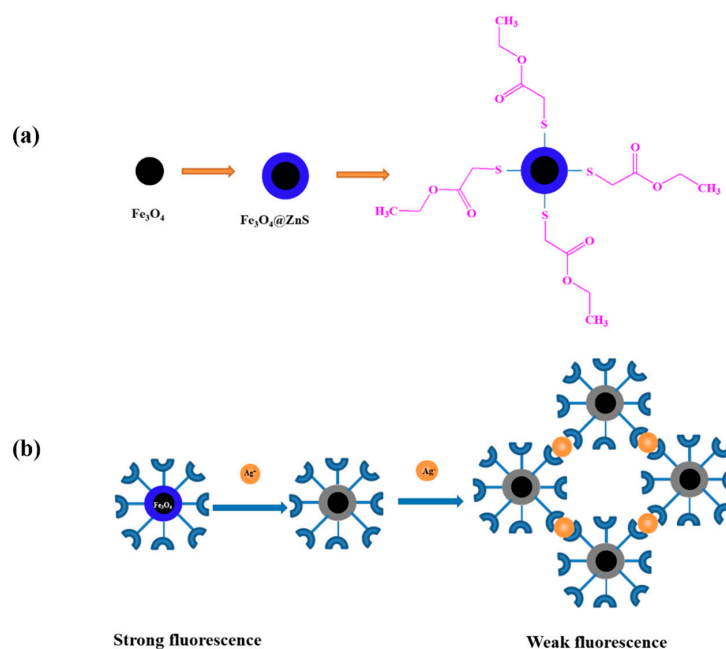


Figure 1. The structure of $\text{Fe}_3\text{O}_4@\text{ZnS}@\text{Ethyl thioglycolate}$ magnetic nanoparticles (a) and the recognition property of magnetic fluorescence nanoprobe $\text{Fe}_3\text{O}_4@\text{ZnS-SH}$ for Ag^+ (b).

2. Experimental

2.1. Materials and Reagents

Iron (III) chloride hexahydrate (99%), iron dichloride (99%), sodium acetate trihydrate (99%), zinc acetate (99%), sodium sulfide (99%), polyethylene glycol 2000, and ethyl thioglycolate (97%) were purchased from Sigma Aldrich.

2.2. Physical Characterizations

Scanning electron microscope (SEM) images were captured by JSM6490LV (JEOL, Tokyo, Japan). Transmission electron microscopy (TEM) images were captured by JEM 2100 (JEOL, Tokyo, Japan). Fourier transform infrared (FTIR) spectroscopy was carried out using Thermo Scientific Nicolet IS50 (ThermoFisher, Waltham, MA, USA). X-ray diffraction (XRD) was performed using on D8FOCUS (Bruker, Karlsruhe, German). X-ray photoelectron spectra (XPS) were obtained using Krayos AXIS Ultra DLDX (Shimadzu, Kyoto, Japan). The magnetic behavior (VSM) was recorded on dried samples by using a 7404 vibrating sample magnetometer (LakeShore, Carson, CA, USA). Thermal gravimetric analysis (TGA) was carried out on a Discovery SDT650 synchronous TGA-DTA instrument (TA, Los Angeles, CA, USA) heated from room temperature to 800 °C (10 °C/min) in nitrogen atmosphere. Lifetime measurements were carried out on FluoroMax-plus instrument (Horiba, Irvine, CA, USA). All fluorescence measurements were performed on a Cary Eclipse spectrophotometer (Varian, Palo Alto, CA, USA). The excitation wavelength was 370 nm and the excitation and emission slit width was set as 10/10 nm.

2.3. Synthesis of Fe₃O₄ Magnetic Nanoparticles

Fe₃O₄ magnetic nanoparticles were synthesized by means of the hydrothermal method reported in the literature. Ferric chloride hexahydrate (2.7 g) was first dissolved with ethanediol (60 mL) in a beaker (100 mL, 85 °C water bath). The mixed solution was stirred, and a black solution was obtained. Then, CH₃COONa (7.2 g) was added to the solution sequentially, the mixed solution was stirred for 30 min and transferred to stainless steel autoclave that lined with polytetrafluoroethylene (100 mL, 200 °C, 12 h). The autoclave was cooled to 25 °C after the reaction. The black products were collected, washed with ethanol for 3 times, and dried at 80 °C for 6 h.

2.4. Synthesis of Fe₃O₄@ZnS Magnetic Nanoparticles

Fe₃O₄ magnetic nanoparticles (0.3 g) were dispersed in deionized water and ammonia (5 mL) to the final volume of 100 mL. The solution was stirred for 30 min in the water bath (80 °C). Then, the mixed solution was injected with the solutions of Zn(Ac)₂·2H₂O (2.5 mmol, 50 mL) and Na₂S·9H₂O (2.5 mmol, 50 mL) and continuously stirred for 6 h in a water bath (80 °C). After the reaction, the products were washed with water several times and further dried at 80 °C for 6 h. Fe₃O₄@ZnS nanoparticles were eventually obtained.

2.5. Synthesis of Fe₃O₄@ZnS@Ethyl Thioglycolate Magnetic Nanoparticles

Fe₃O₄@ZnS microspheres (30 mg) were dispersed in a mixed solution system (1 mL chloroform, 1 mL water and 1 mL ethyl thioglycolate) and the mixture was left until it was divided into two layers of solution. The upper solution was removed and was added with alcohol (1 mL) to deposit the Fe₃O₄@ZnS@Ethyl thioglycolate nanoparticles. The product was treated with a centrifuge for 30 min (8000 rpm) and added to water (1 mL) and NaOH, and then was filtered by filter membrane. Alcohol (1 mL) was added to the filtered solution and centrifuged for 30 min (8000 rpm). Finally, the product was dried at 80 °C for 6 h. Fe₃O₄@ZnS@ Ethyl thioglycolate (Fe₃O₄@ZnS-SH) nanoparticles were eventually obtained.

2.6. Determination of Ag⁺ by Magnetic Fluorescence Nanoprobe Fe₃O₄@ZnS-SH

Before the spectroscopic measurements, the working solutions of the magnetic fluorescence nanoprobe Fe₃O₄@ZnS-SH (1 mg/mL) and different concentrations of AgNO₃ (0–400 μM) were prepared by diluting the high concentration solution to the required

concentration. To investigate the selectivity of the magnetic fluorescence nanoprobe $\text{Fe}_3\text{O}_4@\text{ZnS-SH}$ toward Ag^+ , the following metal ion salts Co^{2+} , Ni^{2+} , Al^{3+} , Cu^{2+} , Zn^{2+} , Cd^{2+} , Fe^{3+} , Fe^{2+} , K^+ , Ca^{2+} , Na^+ , Pb^{2+} , and Hg^{2+} were used. All spectra were collected three times to eliminate the error induced by the suspension change and instrument fluctuation.

3. Results and Discussion

3.1. SEM and TEM Analysis

SEM and TEM analyses of Fe_3O_4 , $\text{Fe}_3\text{O}_4@\text{ZnS}$, and $\text{Fe}_3\text{O}_4@\text{ZnS}@\text{Ethyl thio glycolate}$ magnetic nanoparticles were conducted to provide the morphological changes of the samples more directly and intuitively during synthesis. The SEM and TEM images of Fe_3O_4 , $\text{Fe}_3\text{O}_4@\text{ZnS}$, and $\text{Fe}_3\text{O}_4@\text{ZnS}@\text{Ethyl thio glycolate}$ magnetic nanoparticles are shown in Figure 2. As shown in Figure 2a,d, the surface of Fe_3O_4 was relatively smooth and flat. Additionally, a thin ZnS layer was formed on the surface when Fe_3O_4 nanoparticles were coated with ZnS (Figure 2b,e), leading to the particle diameter becoming larger and the dispersity being improved. The smaller-diameter particles that were scattered around were some residual ZnS quantum dots. After the reaction of ethyl thio glycolate on the surface of $\text{Fe}_3\text{O}_4@\text{ZnS}$ (Figure 2c,f), the surface of the $\text{Fe}_3\text{O}_4@\text{ZnS}@\text{Ethyl thio glycolate}$ magnetic nanoparticles' structure was more uniform and smoother than $\text{Fe}_3\text{O}_4@\text{ZnS}$, and the volume increased, confirming the successful synthesis of $\text{Fe}_3\text{O}_4@\text{ZnS}@\text{Ethyl thio glycolate}$.

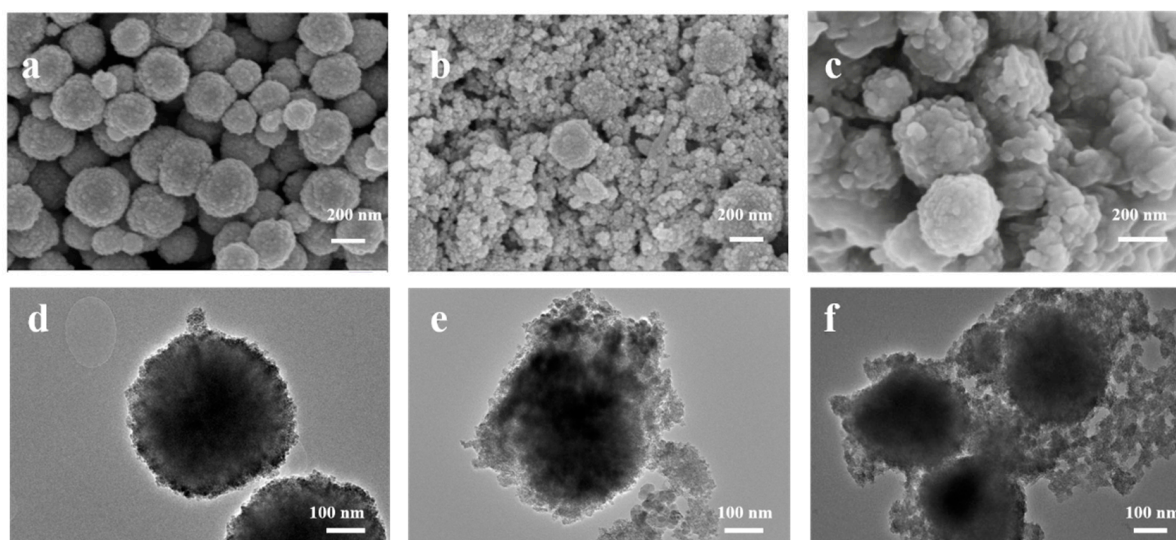


Figure 2. The SEM images of (a) Fe_3O_4 , (b) $\text{Fe}_3\text{O}_4@\text{ZnS}$, and (c) $\text{Fe}_3\text{O}_4@\text{ZnS}@\text{Ethyl thio glycolate}$ and TEM images of (d) Fe_3O_4 , (e) $\text{Fe}_3\text{O}_4@\text{ZnS}$, and (f) $\text{Fe}_3\text{O}_4@\text{ZnS}@\text{Ethyl thio glycolate}$.

3.2. Characterization of $\text{Fe}_3\text{O}_4@\text{ZnS}@\text{Ethyl Thio glycolate}$ Magnetic Nanoparticles

First, the FT-IR spectra of Fe_3O_4 , $\text{Fe}_3\text{O}_4@\text{ZnS}$, $\text{Fe}_3\text{O}_4@\text{ZnS}@\text{Ethyl thio glycolate}$ ($\text{Fe}_3\text{O}_4@\text{ZnS-SH}$) and ethyl thio glycolate are shown in Figure 3. As is shown in the spectra of Fe_3O_4 , the absorption peaks at 3436 cm^{-1} and 1562 cm^{-1} belong to $-\text{OH}$ and $\text{C}=\text{C}$, respectively [40]. The strong characteristic absorption peak at 584 cm^{-1} is due to the stretching vibration of Fe-O . The peak at 1420 cm^{-1} was attributed to C-O tensile vibration, and the peak at 1652 cm^{-1} may be due to existing generated carbonyl group from the transformation of some parts of polyethylene glycol, which indicated the presence of surfactant in the product. As for the spectra of $\text{Fe}_3\text{O}_4@\text{ZnS}$, the absorption peaks at 580 cm^{-1} and 627 cm^{-1} represent Fe-O and Zn-S , respectively. The $-\text{SH}$ bond stretching vibration peaks from ethyl thio glycolate are located at $2600\text{--}2500\text{ cm}^{-1}$ and disappeared in the spectra of $\text{Fe}_3\text{O}_4@\text{ZnS}@\text{Ethyl thio glycolate}$. Compared with the FT-IR spectroscopy of ethyl thio glycolate, the disappearance of the characteristic absorption peak of the $-\text{SH}$ stretching vibration in $\text{Fe}_3\text{O}_4@\text{ZnS}@\text{Ethyl thio glycolate}$ also confirmed the successful combination of

the ethyl thioglycolate and $\text{Fe}_3\text{O}_4@ZnS$. These results prove that the $\text{Fe}_3\text{O}_4@ZnS@$ Ethyl thioglycolate magnetic nanoparticles were successfully synthesized.

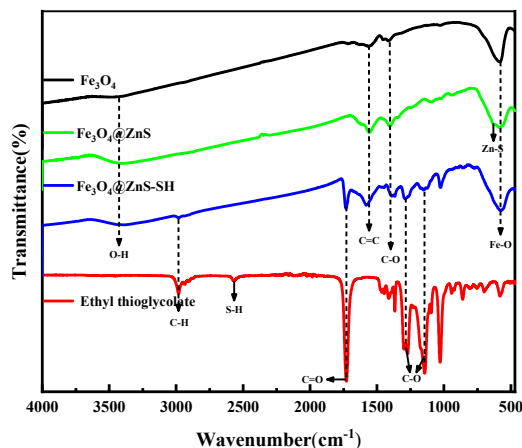


Figure 3. FT–IR spectra of Fe_3O_4 , $\text{Fe}_3\text{O}_4@ZnS$, $\text{Fe}_3\text{O}_4@ZnS@$ Ethyl thioglycolate and ethyl thioglycolate.

Secondly, XRD technology was applied to analyze the structural patterns of ZnS , Fe_3O_4 , $\text{Fe}_3\text{O}_4@ZnS$ and $\text{Fe}_3\text{O}_4@ZnS@$ Ethyl thioglycolate nanoparticles (Figure 4) and the XRD diffraction patterns of the ZnS , Fe_3O_4 , $\text{Fe}_3\text{O}_4@ZnS$ and $\text{Fe}_3\text{O}_4@ZnS@$ Ethyl thioglycolate structure were compared. In Figure 4, the data for ZnS nanoparticles showed the diffraction peaks at $2\theta = 28.9^\circ$, 47.7° , and 57.0° , which can be indexed to the (111), (220), and (311) planes of ZnS , respectively. Additionally, the data for Fe_3O_4 nanoparticles showed the diffraction peaks at $2\theta = 30.1^\circ$, 35.6° , 43.1° , 57.1° , and 62.8° , which can be indexed to the (220), (311), (222), (511), and (440) planes of Fe_3O_4 , respectively [41]. In addition, these diffraction peaks did not change in the XRD patterns of $\text{Fe}_3\text{O}_4@ZnS$ and $\text{Fe}_3\text{O}_4@ZnS-SH$. The surface modification of the magnetic nanoparticles introduced no change in the crystal structure and the data indicated the stability of the Fe_3O_4 . Thereby, the results demonstrated that the ZnS and ethyl thioglycolate were successfully coated onto the surface of the Fe_3O_4 nanoparticles.

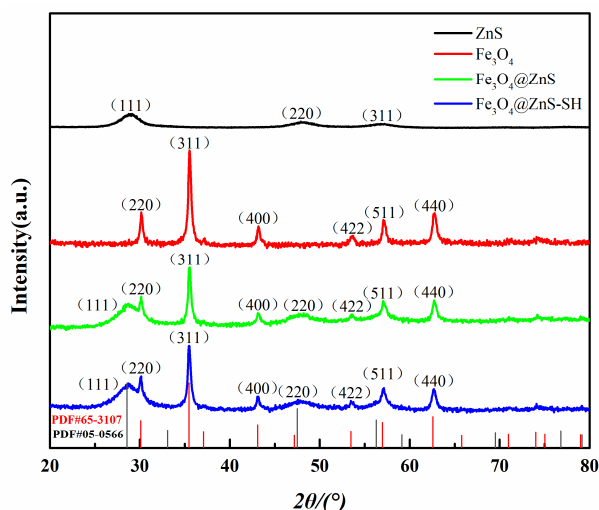


Figure 4. XRD patterns of ZnS , Fe_3O_4 , $\text{Fe}_3\text{O}_4@ZnS$ and $\text{Fe}_3\text{O}_4@ZnS@$ Ethyl thioglycolate.

Next, the results of elemental analysis using XPS in Figure 5a confirmed the difference between Fe_3O_4 , $\text{Fe}_3\text{O}_4@ZnS$ and $\text{Fe}_3\text{O}_4@ZnS-SH$. The peaks of $\text{Fe}2p$ (725 eV, 708 eV), $\text{O}1s$ (530 eV), and $\text{C}1s$ (283 eV) that appeared in $\text{Fe}_3\text{O}_4@ZnS@$ Ethyl thioglycolate were also observed in $\text{Fe}_3\text{O}_4@ZnS$ and Fe_3O_4 , while additional peaks of $\text{Zn}2p$ (1019 eV, 1042 eV)

and S2p (159 eV) were also observed in Fe₃O₄@ZnS and Fe₃O₄@ZnS-SH, which were seen more clearly in the XPS Zn2p and XPS S2p shown in Figure 5c,d [42]. Due to the core-shell structure of nanoparticles, the intensities of the outer shell component lines of O and C decreased in turn and the intensities of the component lines of Zn and S decreased in turn.

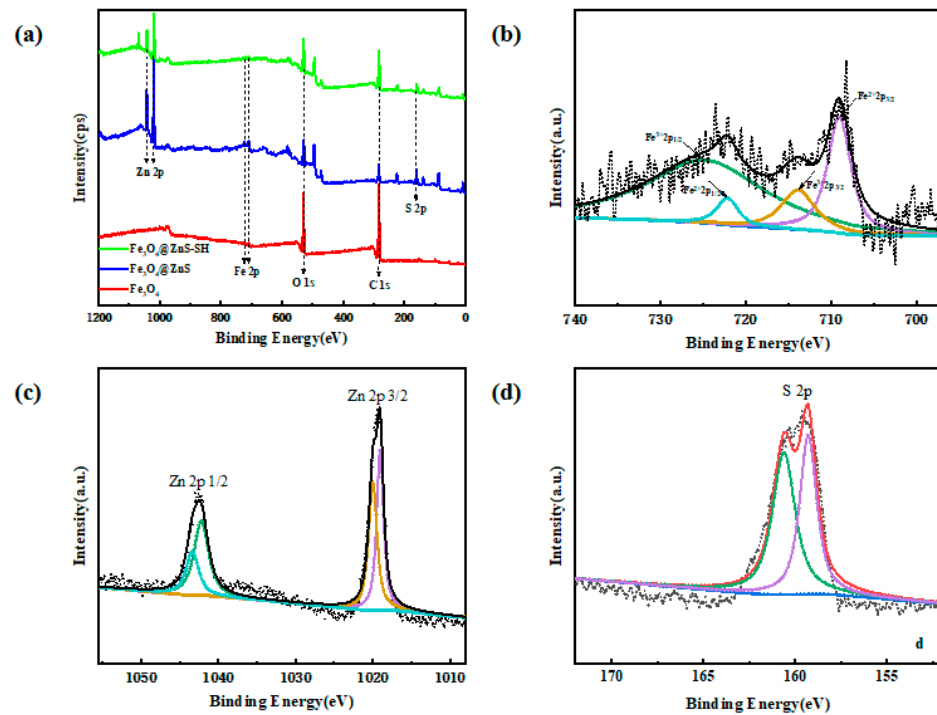


Figure 5. XPS analysis of Fe₃O₄, Fe₃O₄@ZnS and Fe₃O₄@ZnS@Ethyl thioglycolate (a). High-resolution XPS spectra of Fe2p (b), Zn2p (c), and S2p (d) of Fe₃O₄@ZnS@Ethyl thioglycolate.

The characteristic Fe2p lines of Fe₃O₄ are presented in Figure 5b, positioned at 709.01 eV and 722.12 eV in the case of Fe²⁺ and at 713.95 eV and 724.95 eV for Fe³⁺, respectively. In addition, in the deconvolution of the Zn2p doublet spectrum (Figure 5c), two components were observed. The peaks positioned at 1019.02 eV and 1042.03 eV and 1021.51 eV and 1044.41 eV were ascribed to 2p (3/2) and 2p (1/2), respectively. Meanwhile, the peaks that were positioned at 159.35 eV and 161.47 eV (Figure 5d) were assigned to metal sulfide S²⁻ (2p3/2 and S 2p1/2) from ZnS, respectively [43]. Therefore, the above results proved the successful modification of ethyl thioglycolate on Fe₃O₄@ZnS.

Then, the magnetic hysteresis (M(H)) loops of three nanoparticles (Fe₃O₄, Fe₃O₄@ZnS and Fe₃O₄@ZnS@Ethyl thioglycolate) were measured in external fields between -20 kG and 20 kG (Figure 6). The results showed that these three nanoparticles had similar M(H) loops with almost complete reversibility, except for the fact that there were small distinctions in the magnetization saturation values. The magnetization saturation value of the Fe₃O₄@ZnS (33 emu/g) was lower than that of the Fe₃O₄ nanoparticles (63 emu/g) because the introduction of the ZnS enhanced the weight of the nanoparticles [44,45]. Similarly, the magnetization saturation value of Fe₃O₄@ZnS@Ethyl thioglycolate (25 emu/g) was the lowest because of the effect of the outer ZnS layer and ethyl thioglycolate. The magnetism of nanomaterials is an important parameter for magnetic materials if they are to be used in rapid separation techniques. So, the excellent reversibility and magnetization saturation value of the Fe₃O₄@ZnS@Ethyl thioglycolate nanoparticles implied that this nanoparticle may be perfect for use to identify heavy metals and separate them from the test environment for recovery. In addition, Figure 6 (inset figure) shows that the Fe₃O₄@ZnS@Ethyl thioglycolate nanoparticles can be easily dragged to the side using an external magnet, and the solution became transparent immediately, demonstrating that

the $\text{Fe}_3\text{O}_4@\text{ZnS}@\text{Ethyl thiolglycolate}$ nanoparticles possess the favorable magnetic ability required to realize the targeted identification and separation.

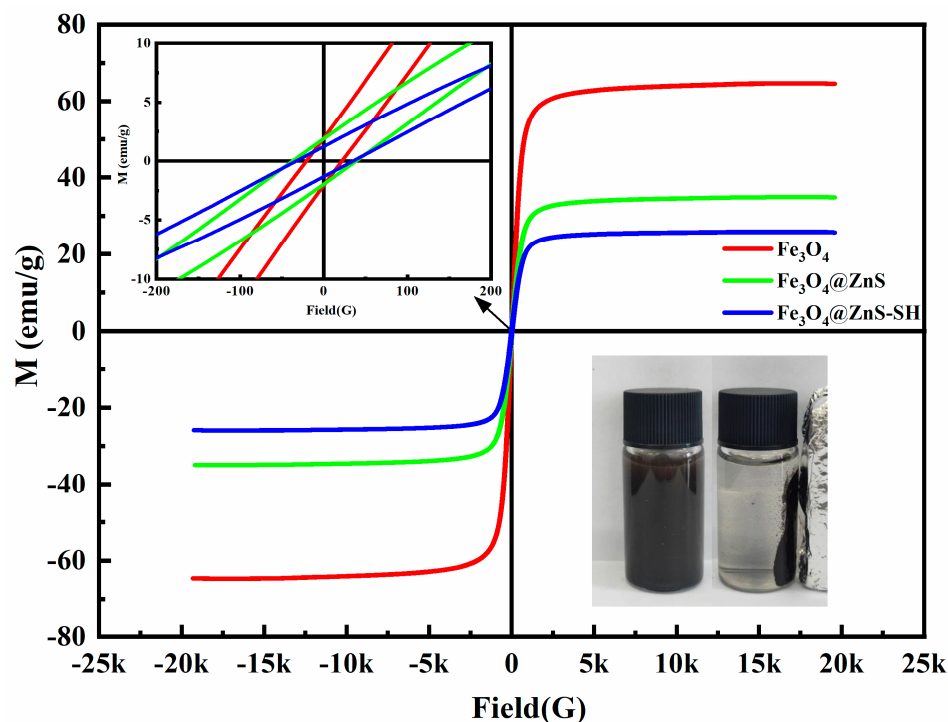


Figure 6. VSM measurements of Fe_3O_4 , $\text{Fe}_3\text{O}_4@\text{ZnS}$ and $\text{Fe}_3\text{O}_4@\text{ZnS}@\text{Ethyl thiolglycolate}$.

Finally, to further investigate the characteristics of the synthesized nanoparticles, three samples were burned at temperatures up to $800\text{ }^\circ\text{C}$ for TGA analysis in a nitrogen atmosphere. Figure 7 shows the thermogravimetric analysis results for Fe_3O_4 , $\text{Fe}_3\text{O}_4@\text{ZnS}$ and $\text{Fe}_3\text{O}_4@\text{ZnS}@\text{Ethyl thiolglycolate}$. As shown, the Fe_3O_4 magnetic nanoparticles exhibited excellent thermal stability due to lacking a surface coating, and the mass loss was 8.71%. When Fe_3O_4 magnetic nanoparticles were coated with ZnS, the $\text{Fe}_3\text{O}_4@\text{ZnS}$ microspheres had a mass loss of 12% due to the ZnS layer on the surface. The weight loss of $\text{Fe}_3\text{O}_4@\text{ZnS}@\text{Ethyl thiolglycolate}$ was 22% at $650\text{ }^\circ\text{C}$, and the maximum total loss was reached at $650\text{ }^\circ\text{C}$. Within the range of $400\text{--}700\text{ }^\circ\text{C}$, $\text{Fe}_3\text{O}_4@\text{ZnS}@\text{Ethyl thiolglycolate}$ presented significantly more mass loss than Fe_3O_4 and $\text{Fe}_3\text{O}_4@\text{ZnS}$, ascribed to the further destruction of ethyl thiolglycolate. The above results indicate the successful synthesis of ethyl thiolglycolate on the surface of $\text{Fe}_3\text{O}_4@\text{ZnS}$.

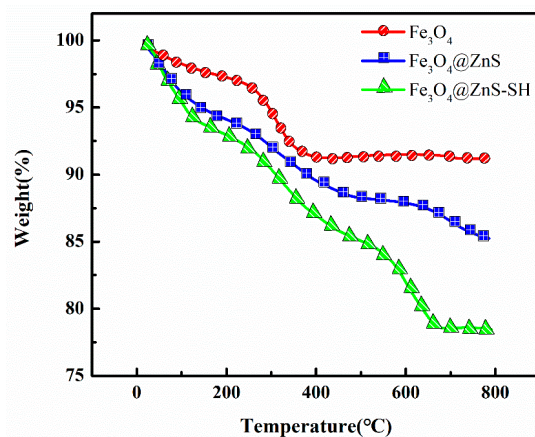


Figure 7. TGA curves of Fe_3O_4 , $\text{Fe}_3\text{O}_4@\text{ZnS}$ and $\text{Fe}_3\text{O}_4@\text{ZnS}@\text{Ethyl thiolglycolate}$.

Combined with the above data, it can be proved that the $\text{Fe}_3\text{O}_4@\text{ZnS}@\text{Ethyl thioglycolate}$ magnetic nanoparticles ($\text{Fe}_3\text{O}_4@\text{ZnS-SH}$) were successfully synthesized.

3.3. Performance Analysis of Magnetic Fluorescence Nanoprobe $\text{Fe}_3\text{O}_4@\text{ZnS-SH}$

Figure 8 showed the comparison of fluorescence characteristic spectra of $\text{Fe}_3\text{O}_4@\text{ZnS}$ and $\text{Fe}_3\text{O}_4@\text{ZnS-SH}$ before and after adding Ag^+ , respectively. It can be seen from Figure 8 that the fluorescence intensity of $\text{Fe}_3\text{O}_4@\text{ZnS}$ is slightly stronger than that of $\text{Fe}_3\text{O}_4@\text{ZnS-SH}$. The addition of Ag^+ can quench both $\text{Fe}_3\text{O}_4@\text{ZnS}$ and $\text{Fe}_3\text{O}_4@\text{ZnS-SH}$. However, it was obvious that the quenching degree of Ag^+ on $\text{Fe}_3\text{O}_4@\text{ZnS-SH}$ is larger than Ag^+ on $\text{Fe}_3\text{O}_4@\text{ZnS}$. It can be concluded that $\text{Fe}_3\text{O}_4@\text{ZnS-SH}$ had a better specific selectivity for Ag^+ , and this magnetic fluorescence nanoprobe could be used to detect Ag^+ . The inset picture presents TEM images of $\text{Fe}_3\text{O}_4@\text{ZnS-SH}$ and that with the addition of Ag^+ , respectively. It can be seen clearly that Ag^+ had been loaded and dispersed on the surface of $\text{Fe}_3\text{O}_4@\text{ZnS-SH}$ magnetic fluorescent nanoparticles. The $\text{Fe}_3\text{O}_4@\text{ZnS-SH}$ nanoparticles themselves had good dispersion and were almost spherical. The complexation of Ag^+ ions and ethyl thioglycolate on the surface of $\text{Fe}_3\text{O}_4@\text{ZnS}$ caused the aggregation of the probe, leading to distinct fluorescence quenching.

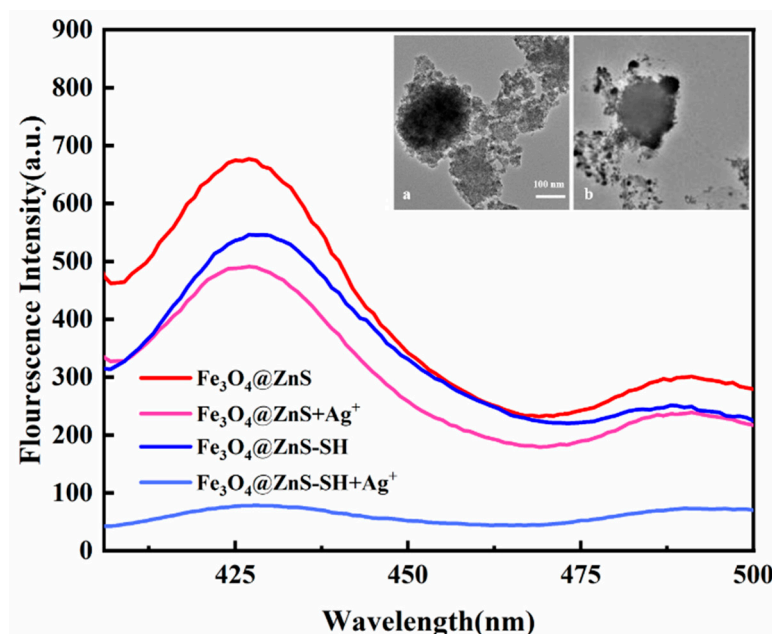


Figure 8. The comparison of the fluorescence spectra of $\text{Fe}_3\text{O}_4@\text{ZnS}$ and $\text{Fe}_3\text{O}_4@\text{ZnS-SH}$ before and after addition of Ag^+ . Inset: TEM images of $\text{Fe}_3\text{O}_4@\text{ZnS-SH}$ (a) and with the addition of Ag^+ (b).

The effect of the concentration of ZnS on the fluorescence intensity of magnetic fluorescence nanoprobe $\text{Fe}_3\text{O}_4@\text{ZnS-SH}$ was investigated. As Figure 9 shows, the fluorescence intensity at 425 nm was increased in the concentration range of 0–12.5 mM. However, the fluorescence intensity decreased as the concentration of ZnS continued to increase. Therefore, the concentration of ZnS was selected at 12.5 mM.

The pH value of the solution is one of the most important parameters affecting the detection ability of the probe. Especially in wastewater, the pH value will decrease with the increase in metal ion concentration. So, the effect of different pH values on the detection results was examined. As shown in Figure 10, the fluorescent intensity and quenching ratio almost did not change as the pH value of the solution varied from 4.0 to 9.0. Hence, the optimal pH value of the solution was chosen as 7.0.

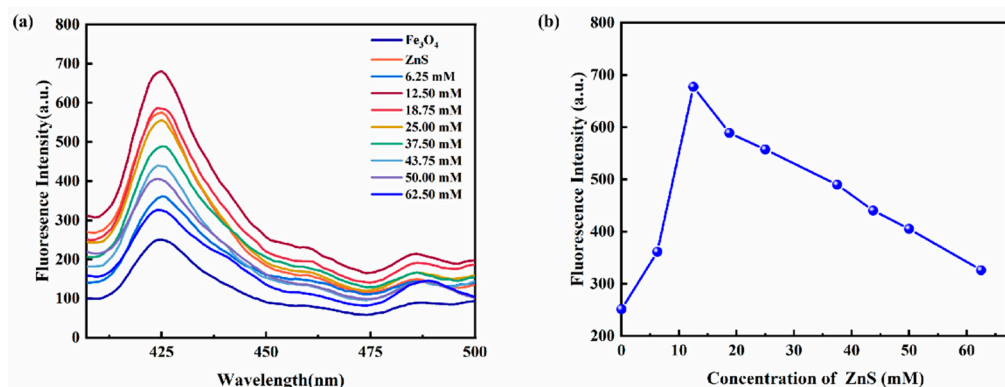


Figure 9. (a) The emission spectra of Fe₃O₄@ZnS at different concentrations of ZnS; (b) the effect of the ZnS concentration on the fluorescence intensity of Fe₃O₄@ZnS.

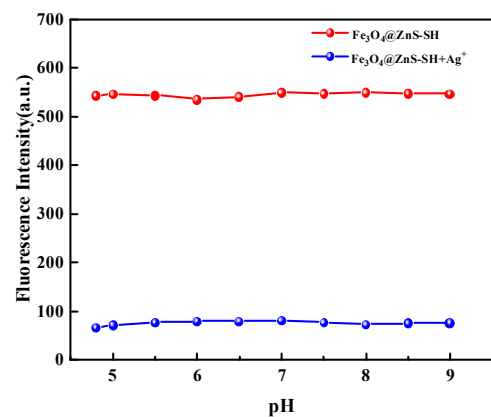


Figure 10. Fluorescence intensity of Fe₃O₄@ZnS-SH in the absence and presence of Ag⁺ at different pH values.

The effect of different concentrations of Ag⁺ on the fluorescent intensity of the Fe₃O₄@ZnS-SH under optimized conditions was investigated. As shown in Figure 11a, the fluorescent intensity of the magnetic fluorescence nanoprobe decreased with the addition of increasing Ag⁺ concentration. Additionally, the fluorescent quenching ratio of the magnetic fluorescence nanoprobe linearly varied in the range of 0–400 μM (Figure 11b) with a low detection limit of 0.20 μM (3δ/k). The linear equation was $I_0/I = 0.01514x + 1.0740$ ($R^2 = 0.9961$). Compared with most of the methods reported before, the magnetic fluorescence nanoprobe Fe₃O₄@ZnS-SH had a wide linear range and a highly sensitive response to Ag⁺. The results indicate its superior analytical ability (Table 1).

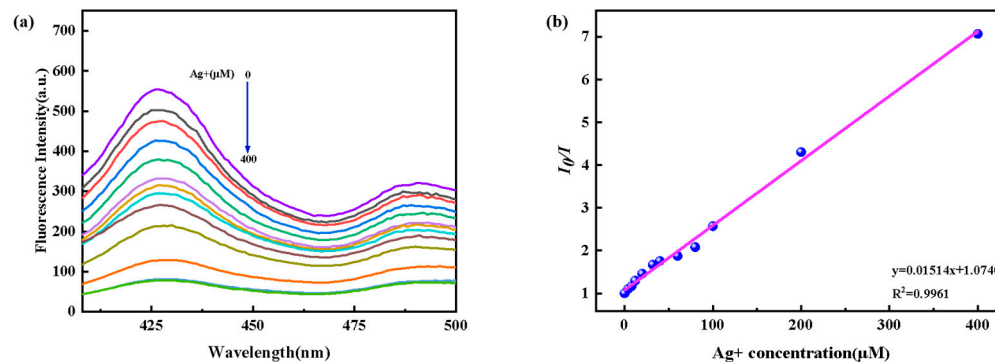


Figure 11. (a) Emission spectra of Fe₃O₄@ZnS-SH in the presence of increasing amounts of Ag⁺ at room temperature; (b) the curve of fluorescence intensity at 425 nm vs. Ag⁺ concentration. The concentrations of Ag⁺ are 0, 4, 8, 12, 20, 32, 40, 60, 80, 100, 200, and 400 μM, respectively.

Table 1. Comparison of the present nanoprobe with other reported sensors for Ag⁺ detection.

Type of Sensor	Detection Range	Detection Limit	Reference
N-doped Ti ₃ C ₂ quantum	0.5–150 μM	0.1 μM	[3]
NPCI-doped carbon quantum dots	15.89–27.66 μM	26.38 μM	[5]
Nitrogen0doped carbon dots	0–40 μM	0.11 μM	[12]
Dual-element-doped carbon quantum dots	0.1–700 μM	0.03 μM	[31]
Acetaldehyde-modified g-C ₃ N ₄ nanosheets	0–30 μM	1.0 μM	[46]
Fe ₃ O ₄ @ZnS-SH	0–400 μM	0.20 μM	This work

According to the World Health Organization standard, the content of silver ions in drinking water should not be higher than 0.05 mg/L, and the concentration of silver ions in human body should be lower than 0.05 mg/L (0.46 μmol/L). The concentration value is just in the linear range, which confirms that the magnetic fluorescent nanoprobe determines the content of silver ions more accurately.

The fluorescence responses of the magnetic fluorescent nanoprobe Fe₃O₄@ZnS-SH to a series of interfering metal ions were recorded to evaluate the probe's selectivity for Ag⁺ recognition (Figure 12a). As shown in Figure 12a, the interfering metal ions induced negligible ratio value changes with the increase in reaction time. However, the fluorescence intensity ratio was significantly increased when adding Ag⁺. These results indicate that the probe could be used in the detection of Ag⁺ specifically.

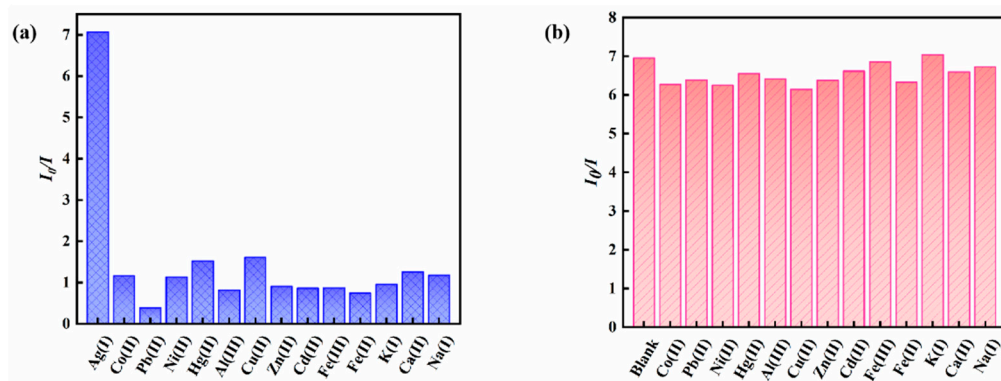


Figure 12. (a) The ratio of fluorescence quenching of Fe₃O₄@ZnS-SH in the presence of different metal ions; (b) the ratio of fluorescence quenching of Fe₃O₄@ZnS-SH upon the addition of Ag⁺ in the presence of other metal ions (Ag⁺, Co²⁺, Ni²⁺, Al³⁺, Cu²⁺, Zn²⁺, Cd²⁺, Fe³⁺, Fe²⁺, K⁺, Ca²⁺, Na⁺ (400 μM); Pb²⁺, Hg²⁺ (40 μM)).

In addition, in the presence of other metal ions, the competitive selectivity of the magnetic fluorescent nanoprobe Fe₃O₄@ZnS-SH was also investigated. As shown in Figure 12b, the magnetic fluorescent nanoprobe Fe₃O₄@ZnS-SH could still respond to Ag⁺ with enhancing fluorescence ratio values, even in the presence of competitive metal ions. These results prove that the magnetic fluorescent nanoprobe Fe₃O₄@ZnS-SH showed high selectivity with Ag⁺ over other metal ions.

Finally, the fluorescence lifetimes of Fe₃O₄@ZnS, Fe₃O₄@ZnS-SH and Fe₃O₄@ZnS-SH with Ag⁺ were studied and compared (Figure 13). The fluorescence lifetime is sensitive to various internal and external factors defined by the fluorophore structure, including temperature, polarity and the presence of fluorescence quenchers. As can be seen from Figure 13, these three samples presented similar exponential decay curves, and the average lifetimes of Fe₃O₄@ZnS, Fe₃O₄@ZnS-SH and Fe₃O₄@ZnS-SH/Ag⁺ systems were 2.79, 3.44

and 3.17 ns, respectively. The fluorescence lifetime measurements showed a much longer decay for Fe₃O₄@ZnS-SH than for Fe₃O₄@ZnS. The considerable improvement in the combination lifetime was primarily attributed to insertion of the ethyl thioglycolate moiety, which controlled the granularity and dispersion of ZnS and led to the longer decay. With the load of Ag⁺, the increases in the non-radiative energy loss competed with normal spontaneous emission processes, which shortened the lifetime of Fe₃O₄@ZnS-SH.

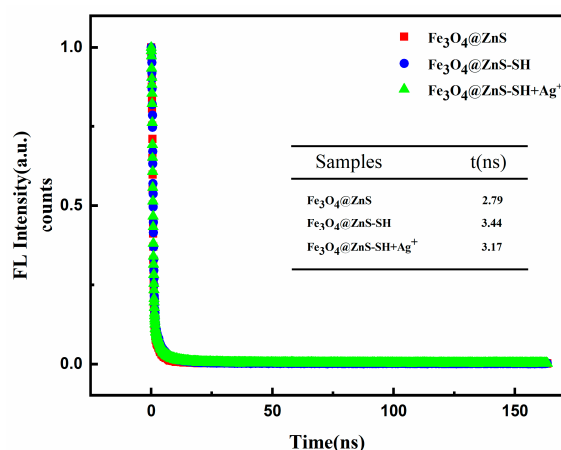


Figure 13. Fluorescence intensity decay curves of Fe₃O₄@ZnS, Fe₃O₄@ZnS-SH and Fe₃O₄@ZnS-SH with the addition of Ag⁺.

3.4. Removal of Ag⁺

Adsorption capacity is an important parameter used to evaluate nanomaterials, and the adsorption capacity of this magnetic fluorescence nanoprobe was investigated. The magnetic fluorescence nanoprobe (0.5 mg) was added to the solution of Ag⁺ (50 mL, 100 μM). After the full reaction of the magnetic fluorescence nanoprobe with Ag⁺, the magnetic fluorescence nanoprobe was separated using an external magnetic field and the concentration of Ag⁺ in the solution was determined with inductively coupled plasma mass spectrometry. The adsorption capacity of this the magnetic fluorescence nanoprobe was calculated using the following equation [47]: $Q = [(C_0 - C) \times V] \times m^{-1}$, where C_0 and C are the initial and final concentrations of Ag⁺ in solution (mg L⁻¹), V is the solution volume (L), and m is the weight of the magnetic fluorescence nanoprobe. The calculated maximum adsorption capacity was about 107.022 mg g⁻¹ and the removal rate of the probe was 99.09%. The comparison of the adsorption capacity of Ag(I) with that of other adsorbents is presented in Table 2. The results show that the adsorption capacity of Fe₃O₄@ZnS-SH was superior to that of most of the adsorbents, suggesting that this magnetic fluorescence nanoprobe could become a potential efficient adsorbent for the removal of Ag(I).

Table 2. Comparison with other reported adsorbents for Ag(I).

Adsorbents	Maximum Adsorption Capacities (mg/g)	Ref.
Fe ₃ O ₄ /polypyrrole nanocomposite	143.3	[48]
Activated carbon/γ-Fe ₂ O ₃ -	32.6	[49]
4,4'-bis-(3-phenylthiourea)diphenyl methane		
Fe ₃ O ₄ @SiO ₂ @TiO ₂ - Ion imprinting polymers	35.48	[50]
Fe ₃ O ₄ @SiO ₂ -HO-S	166.32	[51]
Fe ₃ O ₄ -sulfur-functionalized polyamidoamine	139.32	[52]
Fe ₃ O ₄ @microbial extracellular polymeric substance	47.6	[53]
Fe ₃ O ₄ @ZnS-SH	107.022	This work

3.5. Detection of Ag^+ in Real Samples

To verify the feasibility of our magnetic fluorescent nanoprobe in complex samples, three samples were analyzed using the standard addition method. As shown in Table 3, the recoveries of three different concentrations of Ag^+ ions ranged from 87.00% to 107.50%, with the relative standard deviation (RSD) being less than 4.5%. These results indicate that the magnetic fluorescent nanoprobe could be used for the determination of Ag^+ ions in real samples with accuracy and reliability.

Table 3. Determination of Ag^+ in real samples.

Sample	Added (μM)	Measured (μM)	Recovery (%)	RSD (%)
Tap water	1	0.98	98.00	2.3
	5.0	5.29	105.80	3.1
	10.0	10.30	103.00	2.9
Mineral water	1	1.02	102.00	3.2
	5.0	4.96	99.20	2.7
	10.0	10.75	107.50	2.5
Electrolysis wastewater	1	0.87	87.00	4.5
	5.0	4.43	88.60	3.9
	10.0	8.75	87.50	4.0

3.6. Detection Mechanism

To gain insights into the detection mechanism, FT-IR was performed to identify the specific binding sites between the magnetic fluorescent nanoprobe and Ag^+ . The result can be clearly observed in Figure 14, when the $\text{Fe}_3\text{O}_4@\text{ZnS-SH}$ interacted with Ag^+ , the tensile peak of methoxy (C-O) was changed from 1287 cm^{-1} to 1372 cm^{-1} , while the characteristic absorption peak of C=O moved from 1729 cm^{-1} to 1736 cm^{-1} [54]. Ethyl thioglycolate was chosen to enhance the coordination between the probe and Ag^+ , and the conclusion was supported by the experimental results.

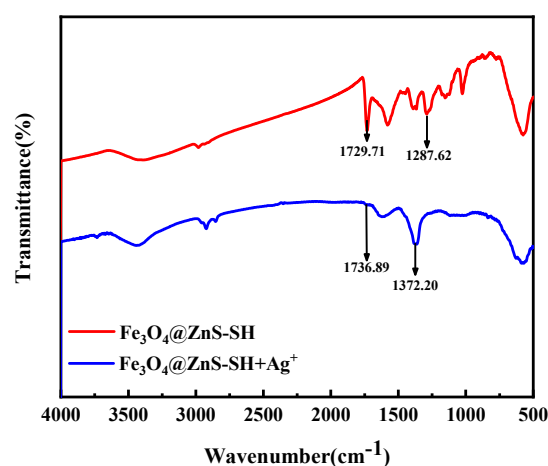


Figure 14. FT-IR spectra of $\text{Fe}_3\text{O}_4@\text{ZnS-SH}$ before and after Ag(I) detection.

4. Conclusions

In summary, ethyl thioglycolate-modified $\text{Fe}_3\text{O}_4@\text{ZnS}$ @Ethyl thioglycolate nanoparticles were successfully synthesized and characterized. A new fluorescence detecting method based on the fluorescence quenching of the $\text{Fe}_3\text{O}_4@\text{ZnS}$ @Ethyl thioglycolate nanoparticle in the presence of Ag^+ was established to determinate Ag^+ with high sensitivity and selectivity. Compared with other detection methods, this magnetic fluorescent nanoprobe provides easy operation and high accuracy and can be successfully used for Ag^+ in practical samples. This magnetic fluorescent nanoprobe provides a new method for enriching, detecting and

separating silver ions, which reduces the pollution of Ag^+ and fluorescence probes in the environment. At the same time, it also provides a new promising platform for the detection of other heavy metal ions.

Author Contributions: Conceptualization, X.Z., M.M. and X.C.; methodology, J.C.; validation, X.C., X.Z. and Z.L.; formal analysis, X.C.; resources, Z.L.; writing—original draft preparation, X.C.; writing—review and editing, X.Z.; supervision, Z.L.; funding acquisition, X.Z., J.C. and S.Y.; All authors have read and agreed to the published version of the manuscript.

Funding: We gratefully acknowledge financial support from Jilin Provincial Department of Science and Technology (202202030205F), the National Natural Science Foundation of China (51902125, 22106051).

Data Availability Statement: The data presented in this study are available upon request from the corresponding author.

Acknowledgments: We gratefully acknowledge financial support from Jilin Provincial Department of Science and Technology, the National Natural Science Foundation of China.

Conflicts of Interest: The authors declare no conflict of interest.

References

1. Carter, S.; Clough, R.; Fisher, A.; Gibson, B.; Russell, B.; Waack, J. Atomic spectrometry update: Review of advances in the analysis of metals, chemicals and materials. *J. Anal. Atom. Spectrom.* **2020**, *35*, 2410–2474. [[CrossRef](#)]
2. Pan, X.-H.; Zu, J.-H.; Diao, J.-J.; Xue, Y.; Liu, S.-Y. Rapid and selective recovery of $\text{Ag}(\text{I})$ from simulative electroplating effluents by sulfhydryl-rich covalent organic framework (COF-SH) with high adsorption capacity. *Colloid. Surface. A* **2022**, *648*, 129156. [[CrossRef](#)]
3. Wang, X.; Zhang, X.-D.; Cao, H.-Y.; Huang, Y.-M. An inorganic base stripping approach to synthesize N-doped Ti_3C_2 quantum dots as fluorescence nanoprobe for the simultaneous detection of Co^{2+} and Ag^+ ions. *Microchem. J.* **2022**, *180*, 107629. [[CrossRef](#)]
4. Carter, S.; Clough, R.; Fisher, A.; Gibson, B.; Russell, B.; Waack, J. Atomic spectrometry update: Review of advances in the analysis of metals, chemicals and materials. *J. Anal. Atom. Spectrom.* **2018**, *33*, 1802–1848. [[CrossRef](#)]
5. Wang, Z.-H.; Zhang, L.; Hao, Y.-M.; Dong, W.-J.; Liu, Y.; Song, S.-M.; Shuang, S.-M.; Dong, C.; Gong, X.-J. Ratiometric fluorescent sensors for sequential on-off-on determination of riboflavin, Ag^+ and L-cysteine based on NPCI-doped carbon quantum dots. *Anal. Chim. Acta* **2021**, *1144*, 1–13. [[CrossRef](#)]
6. Greda, K.; Welna, M.; Pohl, P. Determination of Ag, Bi, Cd, Hg, Pb, Tl, and Zn by inductively coupled plasma mass spectrometry combined with vapor generation assisted by solution anode glow discharge—A preliminary study. *Talanta* **2022**, *246*, 123500. [[CrossRef](#)]
7. Ji, Z.-P.; Shu, Y.; Xu, Q.; Hu, X.-Y. Ultrasensitive electrochemiluminescence determination of trace Ag ions based on the signal amplification caused by its catalytic effect on Mn(II) oxidation using graphite catheter as electrode. *Talanta* **2018**, *187*, 188–192. [[CrossRef](#)]
8. Çetin, T.; Tokaloğlu, Ş.; Ülgen, A.; Şahan, S.; Özentürk, İ.; Soykan, C. Synthesis/characterization of a new chelating resin and on-line solid phase extraction for the determination of $\text{Ag}(\text{I})$ and $\text{Pd}(\text{II})$ from water, cream, anode slime and converter samples by flow injection flame atomic absorption spectrometry. *Talanta* **2013**, *105*, 340–346. [[CrossRef](#)]
9. Junk, T.; Rehkämper, M.; Laycock, A. High-sensitivity tracing of stable isotope labeled Ag nanoparticles in environmental samples using MC-ICP-MS. *J. Anal. Atom. Spectrom.* **2019**, *34*, 1173–1183. [[CrossRef](#)]
10. Fu, Y.; Yang, Y.-J.; Tuersun, T.; Yu, Y.; Zhi, J.-F. Simple preparation and highly selective detection of silver ions using an electrochemical sensor based on sulfur-doped graphene and a 3,3',5,5'-tetramethylbenzidine composite modified electrode. *Analyst* **2018**, *143*, 2076–2082. [[CrossRef](#)] [[PubMed](#)]
11. Zeng, L.-W.; Wu, M.-F.; Chen, S.; Zheng, R.-Q.; Xing, Y.-R.; He, L.; Duan, Y.-X.; Wang, X. Direct and sensitive determination of Cu, Pb, Cr and Ag in soil by laser ablation microwave plasma torch optical emission spectrometry. *Talanta* **2022**, *246*, 123516. [[CrossRef](#)] [[PubMed](#)]
12. Li, J.-J.; Zuo, G.-C.; Qi, X.-L.; Wei, W.; Pan, X.-H.; Su, T.; Zhang, J.-F.; Dong, W. Selective determination of Ag^+ using Salcan derived nitrogen doped carbon dots as a fluorescent probe. *Mat. Sci. Eng. C* **2017**, *77*, 508–512. [[CrossRef](#)] [[PubMed](#)]
13. Xu, Z.-Y.; Wang, X.-H.; Huang, S.-L.; Chen, J.-R.; Luo, H.-Q.; Li, N.-B. Evolving a high-performance bio-imaging tool derived from a compact fluorophore as well as creating a reaction-based fluorescent probe for precise determination of Ag^+ . *Chem. Eng. J.* **2022**, *457*, 140756. [[CrossRef](#)]
14. Zeng, X.-D.; Chen, X.; Chen, J.; Ma, M.-S.; Jin, H.; Yu, S.-H.; Liu, Z.-G. A simple highly selective ratiometric fluorescent probe for detection of peroxydinitrite and its bioimaging applications. *Dye. Pigment.* **2023**, *210*, 110993. [[CrossRef](#)]
15. Zeng, X.-D.; Chen, J.; Yu, S.-H.; Liu, Z.-G.; Ma, M.-S. A highly selective and sensitive “turn-on” fluorescent probe for Fe^{2+} and its applications. *J. Lumin.* **2022**, *250*, 119069. [[CrossRef](#)]

16. Zeng, X.-D.; Li, Z.-L.; Fu, J.; Jiang, C.; Ma, M.-S.; Zhu, L.; Jin, X. A novel ultrasensitive peroxyxynitrite-specific fluorescent probe and its bioimaging applications in living systems. *Dye. Pigment.* **2021**, *186*, 108982. [[CrossRef](#)]
17. Zeng, X.-D.; Jiang, C.; Zhang, Q.; Chai, D.-K.; Ma, M.-S.; Chen, J.-Z.; Liu, G. A novel simple fluorescent probe for the detection of hydrogen peroxide in vivo with high selectivity. *J. Lumin.* **2021**, *240*, 118422. [[CrossRef](#)]
18. Mastracco, P.; González-Rosell, A.; Evans, J.; Bogdanov, P.; Copp, S.M. Chemistry-Informed Machine Learning Enables Discovery of DNA-Stabilized Silver Nanoclusters with Near-Infrared Fluorescence. *ACS Nano* **2022**, *16*, 16322–16331. [[CrossRef](#)]
19. Wang, Z.-X.; Tang, C.-M.; Huang, M.-M.; Rong, X.; Lin, H.-Q.; Su, R.-X.; Wang, Y.-F.; Qi, W. One-Step Synthesis of Peptide- Gold Nanoclusters with Tunable Fluorescence and Enhanced Gene Delivery Efficiency. *Langmuir* **2022**, *38*, 14799–14807. [[CrossRef](#)]
20. Xia, L.P.; Zhang, X.N.; Chen, Y.; Peng, J.; Liu, M.-R.; Huo, D.-Z.; Li, G.-Y.; He, H. A fluorescence turn-on strategy to achieve detection of captopril based on Ag nanoclusters. *Chem. Phys. Lett.* **2022**, *807*, 140085. [[CrossRef](#)]
21. Yuan, C.; Liu, B.-H.; Liu, F.; Han, M.-Y.; Zhang, Z.-P. Fluorescence “Turn On” Detection of Mercuric Ion Based on Bis(dithiocarbamate)copper(II) Complex Functionalized Carbon Nanodots. *Anal. Chem.* **2014**, *86*, 1123–1130. [[CrossRef](#)]
22. Maestro, L.M.; Rodríguez, E.M.; Rodríguez, F.S.; Iglesias-de la Cruz, M.C.; Juarranz, A.; Naccache, R.; Vetrone, F.; Jaque, D.; Capobianco, J.A.; Solé, J.G. CdSe Quantum Dots for Two-Photon Fluorescence Thermal Imaging. *Nano Lett.* **2010**, *10*, 5109–5115. [[CrossRef](#)] [[PubMed](#)]
23. Schulz, A.S.; Hartevelde, C.A.M.; Vancso, G.J.; Huskens, J.; Cloetens, P.; Vos, W.L. Targeted Positioning of Quantum Dots Inside 3D Silicon Photonic Crystals Revealed by Synchrotron X-ray Fluorescence Tomography. *ACS Nano* **2022**, *16*, 3674–3683. [[CrossRef](#)]
24. Das, P.; Biswas, S.; Bhattacharya, S.S.; Nath, P. Carbon Nanodot-Neutral Red-Based Photometric and Fluorescence Sensing for Trace Detection of Nitrite in Water and Soil Using Smartphone. *ACS Appl. Nano Mater.* **2022**, *5*, 3265–3274. [[CrossRef](#)]
25. Guo, X.-R.; Yang, J.; Wei, Y.-B.; Wang, L.-S.; Pi, J. Graphitic Carbon Nitride Quantum Dots in Dual-Mode Fluorescence Switching Platforms for Trace Analysis of Ag(I) and L-Cysteine. *ACS Appl. Nano Mater.* **2022**, *5*, 4230–4240. [[CrossRef](#)]
26. Yang, B.; He, X.-Y.; Xu, H.-F.; Yao, J.-X.; Li, G. Ultrasensitive visualization detection of sodium borohydride based on surface treated transparent molybdenum oxide quantum dots. *Mater. Lett.* **2023**, *331*, 133431. [[CrossRef](#)]
27. Li, Y.-C.; Jia, W.-X.; Yang, Z.-P.; Yang, J.; Chen, Y.-Y.; Yang, J.-Q.; Zhang, W.; Lu, C.-F.; Wang, X.-X. A fluorescent and colorimetric probe for MoO₄²⁻-based on sulfur quantum dots nanozyme. *J. Alloys Compd.* **2023**, *934*, 167926. [[CrossRef](#)]
28. Dhandapani, E.; Maadeswaran, P.; Raj, R.M.; Raj, V.; Kandiah, K.; Duraisamy, N. A potential forecast of carbon quantum dots (CQDs) as an ultrasensitive and selective fluorescence probe for Hg (II) ions sensing. *Mat. Sci. Eng.* **2023**, *287*, 116098. [[CrossRef](#)]
29. Wang, H.-L.; Zhu, W.-J.; Fang, M.; Xu, Y.; Li, C. Turn-on fluorescence probe for high sensitive and selective detection of Ag⁺ by L-glutathione capped CdTe quantum dots in aqueous medium. *J. Lumin.* **2016**, *180*, 14–19. [[CrossRef](#)]
30. Lou, Y.; Sun, W.; Jiang, L.; Fan, X.-G.; Zhang, K.-Y.; Chen, S.-P.; Li, Z.-Y.; Ji, J.-Y.; Ou, J.; Liao, L.; et al. Double-enhanced fluorescence of graphene quantum dots from cane molasses via metal and PEG modification for detecting metal ions and pigments. *Opt. Mater.* **2022**, *133*, 113037. [[CrossRef](#)]
31. Dong, W.-Y.; Yan, J.-Q.; Wu, Q.-S.; Hu, X.-J. A fluorescent probe constructed of water-soluble dual-element-doped carbon quantum dots for rapid and highly sensitive detection of Ag⁺. *Inorg. Chem. Commun.* **2021**, *134*, 109052. [[CrossRef](#)]
32. Shalali, F.; Cheraghi, S.; AliTaher, M. A sensitive electrochemical sensor amplified with ionic liquid and N-CQD/Fe₃O₄ nanoparticles for detection of raloxifene in the presence of tamoxifen as two essentials anticancer drugs. *Mater. Chem. Phys.* **2022**, *278*, 125658. [[CrossRef](#)]
33. Wang, L.; Huang, X.-Y.; Wang, C.-Q.; Tian, X.-Y.; Chang, X.-H.; Ren, Y.; Yu, S.S. Applications of surface functionalized Fe₃O₄ NPs-based detection methods in food safety. *Food Chem.* **2021**, *342*, 128343. [[CrossRef](#)]
34. Hatami, M.; Mohammadi-Rezaei, S.; Tahari, M.; Jing, D. Recent developments in magneto-hydrodynamic Fe₃O₄ nanofluids for different molecular applications: A review study. *J. Molecul. Liq.* **2018**, *250*, 244–258. [[CrossRef](#)]
35. Rakhtshah, J. A comprehensive review on the synthesis, characterization, and catalytic application of transition-metal Schiff-base complexes immobilized on magnetic Fe₃O₄ nanoparticles. *Coordin. Chem. Rev.* **2022**, *467*, 214614. [[CrossRef](#)]
36. Nafchi, R.F.; Ahmadi, R.; Heydari, M.; Rahimpour, M.R.; Molaei, M.J.; Unsworth, L. In Vitro Study: Synthesis and Evaluation of Fe₃O₄/CQD Magnetic/Fluorescent Nanocomposites for Targeted Drug Delivery, MRI, and Cancer Cell Labeling Applications. *Langmuir* **2022**, *38*, 3804–3816. [[CrossRef](#)] [[PubMed](#)]
37. Koc, K.; Karakus, B.; Rajar, K.; Alveroglu, E. Synthesis and Characterization of ZnS@Fe₃O₄ Fluorescent-Magnetic Bifunctional Nanospheres. *Superlattices Microstruct.* **2017**, *110*, 198–204. [[CrossRef](#)]
38. Song, X.-J.; Yang, F.; Fang, Q.-L.; Hu, H.-M.; Xu, F. Synthesis of Magnetic MWNTs/ZnS/Fe₃O₄ Nanocomposites and Their Enhanced Photocatalytic Activity. *Synth. React. Inorg. M.* **2016**, *46*, 638–641. [[CrossRef](#)]
39. Ding, Y.-D.; Sun, Y.-W.; Hong, X.; Cong, T.; Wen, X.-K.; Zhao, H.-Y. Fabrication of Fe₃O₄/ZnS nanocomposites towards ultrasensitive resonant Raman scattering-based immunoassays. *Mater. Lett.* **2019**, *253*, 354–357. [[CrossRef](#)]
40. Mondal, D.K.; Phukan, G.; Paul, N.; Borah, J.P. Improved self heating and optical properties of bifunctional Fe₃O₄/ZnS nanocomposites for magnetic hyperthermia application. *J. Magn. Magn. Mater.* **2021**, *528*, 167809. [[CrossRef](#)]
41. Dafeh, S.R.; Iranmanesh, P.; Salarizadeh, P. Fabrication, optimization, and characterization of ultra-small superparamagnetic Fe₃O₄ and biocompatible Fe₃O₄@ZnS core/shell magnetic nanoparticles: Ready for biomedicine applications. *Mat. Sci. Eng. C* **2019**, *98*, 205–212. [[CrossRef](#)]
42. Stefan, M.; Leostean, C.; Pana, O.; Soran, M.L.; Suci, R.C.; Gautron, E.; Chauvet, O. Synthesis and characterization of Fe₃O₄@ZnS and Fe₃O₄@Au@ZnS core-shell nanoparticles. *Appl. Surf. Sci.* **2014**, *288*, 180–192. [[CrossRef](#)]

43. Feng, L.-P.; Zhang, L.-X.; Chen, X.; Zhang, C.-X.; Mao, G.-J.; Wang, H. A visible light-driven photoelectrochemical sensor for mercury (II) with “turn-on” signal output through in-situ formation of double type-II heterostructure using CdS nanowires and ZnS quantum dots. *Chem. Eng. J.* **2022**, *441*, 136073. [[CrossRef](#)]
44. Gerulová, K.; Kucmanová, A.; Sanny, Z.; Garaiová, Z.; Seiler, E.; Čaplovičová, M.; Čaplovič, L.; Palcut, M. Fe₃O₄-PEI Nanocomposites for Magnetic Harvesting of *Chlorella vulgaris*, *Chlorella ellipsoidea*, *Microcystis aeruginosa*, and *Auxenochlorella protothecoides*. *Nanomaterials* **2022**, *12*, 1786. [[CrossRef](#)] [[PubMed](#)]
45. Savvidou, M.G.; Dardavila, M.M.; Georgiopoulou, I.; Louli, V.; Stamatis, H.; Kekos, D.; Voutsas, E. Optimization of Microalga *Chlorella vulgaris* Magnetic Harvesting. *Nanomaterials* **2021**, *11*, 1614. [[CrossRef](#)] [[PubMed](#)]
46. Cao, S.-H.; Chen, H.; Jiang, F.; Hu, Z.-X.; Wang, X. Construction of Acetaldehyde-Modified g-C₃N₄ Ultrathin Nanosheets via Ethylene Glycol-Assisted Liquid Exfoliation for Selective Fluorescence Sensing of Ag⁺. *ACS Appl. Mater. Interfaces* **2018**, *10*, 44624–44633. [[CrossRef](#)]
47. Zhu, B.-C.; Yang, P.-L.; Yu, H.-Q.; Yan, L.-G.; Wei, Q.; Du, B. Development of a novel water-soluble magnetic fluorescent nanoparticle for the selective detection and removal of Cu²⁺. *Nanotechnology* **2013**, *24*, 495502. [[CrossRef](#)]
48. Peng, X.-Q.; Zhang, W.; Gai, L.-G.; Jiang, H.-H.; Wang, Y.; Zhao, L.-C. Dedoped Fe₃O₄/PPy nanocomposite with high anti-interfering ability for effective separation of Ag(I) from mixed metal-ion solution. *Chem. Eng. J.* **2015**, *218*, 197–205. [[CrossRef](#)]
49. Ghanei-Motlagh, M.; Fayazi, M.; Taher, M.A.; Jalalinejad, A. Application of magnetic nanocomposite modified with a thiourea based ligand for the preconcentration and trace detection of silver(I) ions by electrothermal atomic absorption spectrometry. *Chem. Eng. J.* **2016**, *290*, 53–62. [[CrossRef](#)]
50. Yin, X.-C.; Long, J.; Xi, Y.; Luo, X.-B. Recovery of silver from wastewater using a new magnetic photocatalytic ion-imprinted polymer. *ACS Sustain. Chem. Eng.* **2017**, *5*, 2090–2097. [[CrossRef](#)]
51. Wei, W.; Li, A.; Pi, S.; Wang, Q.; Zhou, L.; Yang, J.; Ma, F.; Ni, B. Synthesis of Core-Shell magnetic nanocomposite Fe₃O₄@microbial extracellular polymeric substances for simultaneous redox sorption and recovery of silver ions as silver nanoparticles. *ACS Sustain. Chem. Eng.* **2018**, *1*, 749–756. [[CrossRef](#)]
52. Zhao, J.-J.; Luan, L.-P.; Li, Z.-W.; Duan, Z.-F.; Li, Y.-F.; Zheng, S.-B.; Xue, Z.-X.; Xu, W.-L.; Niu, Y.-Z. The adsorption property and mechanism for Hg(II) and Ag(I) by Schiff base functionalized magnetic Fe₃O₄ from aqueous solution. *J. Alloys Compd.* **2020**, *825*, 154051. [[CrossRef](#)]
53. Luan, L.-P.; Tang, B.-T.; Liu, Y.-F.; Wang, A.-L.; Zhang, B.-B.; Xu, W.-L.; Niu, Y.-Z. Selective capture of Hg(II) and Ag(I) from water by sulfur-functionalized polyamidoamine dendrimer/magnetic Fe₃O₄ hybrid materials. *Sep. Purif. Technol.* **2021**, *257*, 117902. [[CrossRef](#)]
54. Luo, L.-X.; Ye, Y.; Wang, H.; Liu, Z.; Li, J.-Q. Rapid detection of Ag⁺ in food using cholesteric chiral artificial receptor L5. *Microchem. J.* **2023**, *190*, 108633.

Disclaimer/Publisher’s Note: The statements, opinions and data contained in all publications are solely those of the individual author(s) and contributor(s) and not of MDPI and/or the editor(s). MDPI and/or the editor(s) disclaim responsibility for any injury to people or property resulting from any ideas, methods, instructions or products referred to in the content.